

Yan Zheng · Shun Fujimoto · Akira Rinoshika

# Combining wavelet transform and POD to analyze wake flow

Received: 1 May 2015 / Revised: 14 August 2015 / Accepted: 20 October 2015 / Published online: 16 November 2015  
© The Visualization Society of Japan 2015

**Abstract** To reveal the possibly existed flow phenomena that buried in a two-dimensional symmetric triangle wake, one-dimensional orthogonal wavelet transform and POD are combined to decompose the fluctuating velocity field into different wavelet components and modes. The features of reconstructed flow fields are analyzed in terms of fluctuating energy, time frequency distribution, space correlation and Reynolds shear stress. It is found that the first two wavelet components and POD modes can give representations to the most energetic large-scale structures, contributing about 77 and 73 % to the total fluctuating energy, respectively. Comparing with the first two wavelet components, the first two POD modes are more appropriate to represent the Karman-like vortical structures. The time–frequency and length scale characteristics of wavelet components suggest that frequency behavior can reflect the spatial-related length scale and the wavelet transform can be used to extract turbulent structures of different scales. Similar to the energy distribution, the most significant contributions to the Reynolds shear stresses comes from the large-scale structures that composed of first two wavelet components and POD modes, accounting for 88 and 80 % of the measured maximum Reynolds shear stress, respectively. Due to different classification criterion of wavelet and POD analyses, the combining use of these two methods tends to be more effective for analyzing multi-scale turbulent structures.

**Keywords** PIV · POD · Turbulent structure · Vortex · Wake · Wavelet transform

## 1 Introduction

Flow around a bluff body is significantly important for engineering applications as it plays an important role in energy, momentum, heat, and mass transfer. The wake formed behind bluff body is random in time and space domain, exhibiting complex structures with a wide range of coexisting scales. A typical characteristic of cylinder wake is the quasi-periodical flow that attributed to large-scale vortex shedding behavior (Williamson 1996), which is found to be a function of velocity, cylinder diameter and Reynolds number (Zdravkovich 1997). The oscillating large-scale structure of wake flow usually has dominating spectral

---

Y. Zheng  
School of Automotive and Traffic Engineering, Jiangsu University of Technology, Changzhou 213001, Jiangsu, China

S. Fujimoto · A. Rinoshika (✉)  
Department of Mechanical Systems Engineering, Graduate School of Science and Engineering, Yamagata University,  
4-3-16 Jonan, Yonezawa-shi, Yamagata 992-8510, Japan  
E-mail: rinosika@yz.yamagata-u.ac.jp  
Tel.: +81-238-26-3225

A. Rinoshika  
School of Power and Energy, Northwestern Polytechnical University, 127 West Youyi Road, Xi'an 710072, Shaanxi, China

components in the range of low frequency. However, besides the large-scale structures, it was proved that the turbulent structures of wake consist of a wide range of relatively small scales, such as the secondary vortices (Wei and Smith 1986), Kelvin–Helmholtz vortices (Lin et al. 1996) and longitudinal rib-like structures (Hussain and Hayakawa 1987), which may also be of significance in the wake. The relatively small-scale structures are usually closely related to the unsteady behaviors buried in the mean flow. In order to give a detailed description of wake flow structure, the identification of the energetic large-scale structure and elucidation of relatively small-scale structure is very desirable.

During the past decades, many researchers have made use of the wavelet transforms' ability to provide both the spectral and temporal (or spatial) information of turbulent wake flows, and to identify vortical structures and the flow intermittency in the time–frequency plane. Addison et al. (2001) applied wavelet transform to extract location feature and turbulent statistical analysis in open channel wake flows, and some possible applications such as vortex shedding patterns of bluff bodies were introduced in his study. Indrusiak and Moller (2011) studied the transient turbulent behavior behind a circular cylinder, in which unexpected strong increase of the Strouhal numbers at lower Reynolds numbers were observed by wavelet transform. Alam and Zhou (2008) presented a detailed investigation of Strouhal numbers, forces and flow structures in the wake of two tandem cylinders using wavelet correlation method, and two distinct vortex frequencies were detected behind the downstream cylinder for the first time. On the other hand, orthogonal wavelet multi-resolution technique (Mallat 1989) based on the discrete wavelet transform was used to extract turbulent structures of various scales as well as coherent structures (Farge et al. 2001). As an example, Rinoshika and Zhou (2005a, b) have applied the one-dimensional orthogonal wavelet multi-resolution technique to the analysis of the cylinder wakes, by which turbulent structure were decomposed into a number of wavelet components based on their characteristic or central frequencies. However, to give further understanding of turbulent wake, the decomposed wavelet components can be further investigated in terms of statistical parameters such as fluctuating energy, turbulent spatial scale and Reynolds correlation functions, which will provide new insights into the multi-scale structure of turbulent wake.

The other popular technique used to detect and extract different dynamic behaviors presented in a flow is the proper orthogonal decomposition technique (POD). This approach can be used to extract the most significant structure from an energetic view point; such structure is referred as coherent structure. Since the pioneering work of Lumley (1967), POD analysis has been widely used to elucidate turbulent structure (Cazemier et al. 1998; Graftieux et al. 2001; Noack et al. 2003). They revealed that the first two modes of POD decomposition present similar levels of energy, and are associated with the convection of the large-scale Karman vortices. Delville et al. (1999) applied POD to investigate large-scale structure in the planar mixing layer. Using proper orthogonal decomposition, Cruz et al. (2005) investigated the spatial organization and temporal behavior of the passive controlled wake flow of a half cylinder, a strong link between the Strouhal number, the mean vorticity and the total energy is observed in this study. Durgesh et al. (2013) represented the near-wake behavior using low-order near-wake velocity reconstructions obtained from proper orthogonal decomposition. As mentioned in the above section, the wavelet analysis can also be used to extract large-scale turbulent structure characterized by its central frequency. The large-scale structures extracted by these two approaches have different physical interpretation due to the different classification criterions of them, which have not been previously investigated, thus attracting our interest.

Recently, Weier et al. (2008) extracted dominant features of an electromagnetically forced separated flow by proper orthogonal decomposition and continuous wavelet transform. Wang et al. (2012) perform POD and wavelet analyses on the flow structures of a polymer drag-reducing flow. However, the detailed comparison between these two methods has not been concerned, and little research on turbulent structures by combining wavelet transform with POD has been conducted, thus motivating the present work.

In order to reveal the turbulent wake generated by triangle cylinder in this study, one-dimensional orthogonal wavelet multi-resolution analysis and POD are combined to decompose the fluctuating velocity field, obtained by the high-speed PIV, into different wavelet components and modes. The features of reconstructed flow fields are analyzed in terms of fluctuating energy, time frequency distribution, space correlation and Reynolds shear stress, and the difference between these two methods are discussed.

## 2 Experimental setup

The experiment was conducted in the circulating water channel, which has 400 mm (width)  $\times$  200 mm (height)  $\times$  1000 mm (length) working section. To ensure the flow homogeneity, a settling chamber, a

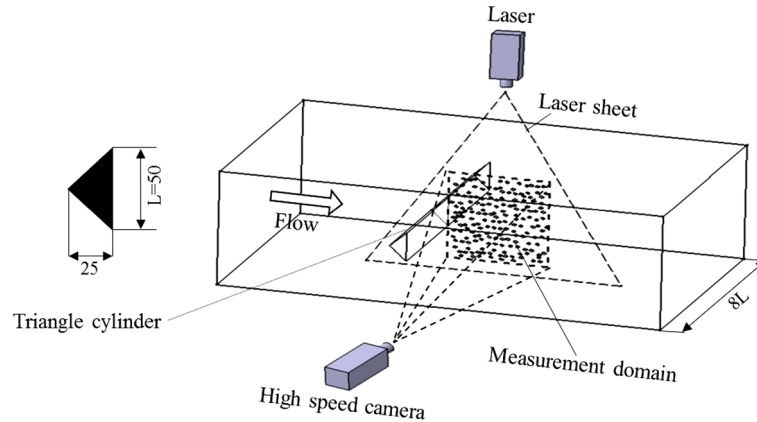


**Fig. 1** Experimental model and measurement setup

honeycomb, three turbulence-damping screens and a contraction were placed in the water channel. As shown in Fig. 1 (left), a two-dimensional symmetric triangle cylinder model, having a scale of  $L = 50$  mm and aspect ratio of 8 with respect to its whole length, was adopted in this study. Concerning the blockage ratio, the classic cases of flow around bluff bodies consider an infinite domain with very small value, but in many cases, it is important to take the effect of blockage ratio into account. Davis et al. (1983) performed experimental and numerical studies on the confined flow around rectangular cylinders at various Reynolds numbers and blockage ratios. They found that the Strouhal number and the drag coefficient increase with the blockage ratio in a wind tunnel. For blockage ratio larger than 6 % in a wind tunnel, West and Apelt (1982) showed that the effects of blockage are complex: the Strouhal number changes with blockage ratio, but drag coefficient is not much different from that of no blockage, which made a correction method unsuitable. Although this experiment is different from the classic case of bluff body in a wind tunnel, we focus on the wake flow structures behind a triangle cylinder with a blockage ratio of 25 % in water channel.

The high-speed PIV measurement, as shown in Fig. 1 (right), was carried out at a constant free-stream velocity of  $U_0 = 0.29$  m/s, which corresponds to Reynolds number of 14,440 in the  $(x, y)$  plane. The turbulence intensity of the circulating water channel was less than 0.5 % of the free-stream velocity.

Polystyrene particles with diameter of 63–75  $\mu\text{m}$  were used as the PIV tracers in the flow loop. A high-speed digital camera (Photron FASTCAM SA3) and a laser light sheet which has a thickness of 1.0 mm were adopted to capture the digital images at a frame rate of 500 fps (frame per second) with a resolution of  $1024 \times 768$  pixels, and the shutter speed of each frame was set at 1 ms. The measurement domain is about  $150 \text{ mm} \times 150 \text{ mm}$  ( $3L \times 3L$ ) behind the cylinder. The velocity field was analyzed by PIV software. Instantaneous velocity vector fields were generated using FFT-based cross-correlation technique between successive particle images. The interrogation window size is  $16 \times 16$  pixels with 50 % overlap, providing 4096 ( $64 \times 64$ ) velocity vectors over the entire measurement domain, and the interval time of two successive images is 2 ms. The statistical uncertainty of the measured velocity field was estimated at  $\pm 1.54$  % at the 95 % confidence level. To determine the time-averaged mean flow structure, 15,000 instantaneous velocity fields were measured in this study.

### 3 Decomposition of velocity field

Before the decomposition, the sequential realizations of velocity field were selected to calculate the fluctuating velocities by subtracting the mean velocity field. The calculation was given by:  $v'(x_i, y_j, n) = v(x_i, y_j, n) - \bar{v}(x_i, y_j)$ ,  $i = 1, \dots, n_x; j = 1, \dots, n_y; n = 1, \dots, n_t$ . Here, the  $v$  denotes streamwise or vertical velocity component, the  $x_i$  and  $y_j$  represents the local spatial positions and the  $n$  is the time sequence of snapshot. The integral time and length scales, based on the auto correlation of fluctuating velocity, were calculated with the value of 0.124 s and 0.037 m, respectively. Then the resulting fluctuating velocities were decomposed by wavelet transform and POD. The implementations of these two approaches will be described in the following subsections.

### 3.1 One-dimensional orthogonal wavelet transform

The wavelet transform can be classified into continuous and orthogonal discrete wavelet transforms. The continuous wavelet transform can provide continuous time–frequency identification of a signal. The orthogonal discrete wavelet transform produces the wavelet coefficients that capture local features of the transformed data in both time and frequency, and the wavelet coefficients are independent and orthogonal to each other. Furthermore, the orthogonal discrete wavelet transform is invertible, enabling the original data to be reconstructed uniquely by using chosen wavelet basis function from the wavelet coefficients of its inverse transform. In this study, the one-dimensional orthogonal discrete wavelet transform using Daubechies wavelet basis  $C^N$  with an order of 8 is adopted and implemented as follows.

$$C^N = \begin{pmatrix} c_0 & c_1 & c_2 & c_3 & \cdots & c_6 & c_7 & 0 & 0 & \cdots & 0 & 0 \\ c_7 & -c_6 & c_5 & -c_4 & \cdots & c_1 & -c_0 & 0 & 0 & \cdots & 0 & 0 \\ 0 & 0 & c_0 & c_1 & \cdots & c_4 & c_5 & c_6 & c_7 & \cdots & 0 & 0 \\ 0 & 0 & c_7 & -c_6 & \cdots & c_3 & -c_2 & c_1 & -c_0 & \cdots & 0 & 0 \\ \cdot & \cdot & \cdot & \cdot & \cdot & \cdot & \cdot & \cdot & \cdot & \cdot & \cdot & \cdot \\ \cdot & \cdot & \cdot & \cdot & \cdot & \cdot & \cdot & \cdot & \cdot & \cdot & \cdot & \cdot \\ c_2 & c_3 & c_4 & c_5 & \cdots & 0 & 0 & 0 & 0 & \cdots & c_0 & c_1 \\ c_5 & -c_4 & c_3 & -c_2 & \cdots & 0 & 0 & 0 & 0 & \cdots & c_7 & -c_6 \end{pmatrix} \quad (1)$$

As evident in the structure of the matrix  $C^N$ , two convolution operations are carried out by multiplying with a data matrix. The odd rows of matrix perform an ordinary convolution with coefficients  $c_0, c_1, c_2, \dots, c_6$  and  $c_7$  acting as a low-pass (smoothing) filter, while the even rows perform a different convolution with coefficients  $c_7, -c_6, c_5, \dots, c_1$  and  $-c_0$  acting as a high-pass (difference) filter.

Considering the one-dimensional data matrix  $v'^N = [v'_1, v'_2, \dots, v'_{2^N}]^T$  formed by the calculated fluctuating velocity at a single measurement point, here the subscripts of  $v'$  denote the time sequences of  $n_t$  ( $n_t = 2048$ ) snapshots, with the index  $N = 11$ . The orthogonal discrete wavelet transform can be expressed in matrix form by

$$S = Wv'^N \quad (2)$$

where  $S$  and  $W$  are discrete wavelet coefficient (or spectrum) matrix and analyzing wavelet matrix of  $v'^N$ , respectively.  $W$  is usually constructed based on a cascade algorithm of orthogonal wavelet basis matrices and the permuting matrices.

$$W = P^4 C^4 \dots P^{N-1} C^{N-1} P^N C^N \quad (3)$$

Here the permuting matrix  $P^N$  is applied to move the odd rows of matrix  $C^N v'^N$  forward as the first  $2^{N-1}$  elements (smooth coefficients) and move the even rows of matrix  $C^N v'^N$  backward as the last  $2^{N-1}$  elements (different coefficients). The wavelet basis matrix  $C^{N-1}$  and the permuting matrix  $P^{N-1}$ , which are the halves of  $C^N$  and  $P^N$ , respectively, are then applied to the first  $2^{N-1}$  smooth elements. This pyramidal procedure is repeated until the last hierarchical level 1 consisting of eight smooth coefficients is obtained. In general, wavelet basis are chosen such that  $W$  satisfies  $W^T W = I$ , where  $I$  is a unit matrix. This condition enables the discrete wavelet transform to be an orthogonal linear operator and invertible. The inverse orthogonal discrete wavelet transform can be simply performed by reversing the procedure:

$$v'^N = W^T S \quad (4)$$

The orthogonal wavelet transform produces coefficients that contain information on the relative local contribution of various frequency bandwidths to the transformed data instead of the frequency components of the original data. In order to obtain the grouped frequency components of the transformed data, the orthogonal wavelet coefficient  $S$  is decomposed into the sum of all levels:

$$S = S_1 + S_2 + S_3 \cdots + S_i + \cdots + S_{N-2} \quad (5)$$

It should be noted that the decomposition levels are determined by the original data length and the selection of wavelet basis. The Daubechies wavelet basis with an order of 8 enables us to perform  $N-3$  times of decomposition, resulting in  $N-2$  levels of wavelet components.

The inverse orthogonal wavelet transform is then applied to the coefficient of each level, viz.

$$v'^N = W^T S_1 + W^T S_2 + W^T S_3 \cdots + W^T S_i + \cdots + W^T S_{N-2}, \quad (6)$$

where terms  $W^T S_1$  and  $W^T S_{N-2}$  represent the data components at wavelet level 1 (the lowest frequency band) and level  $N-2$  (the highest frequency band). It is evident that the fluctuating velocity can be reconstructed by the sum of wavelet components characterized by their frequency bandwidth. This decomposition method is referred to as the wavelet multi-resolution technique.

To perform quantitative analysis on the PIV results, the fluctuating velocities in the measurement plane are decomposed into 9 levels by above-mentioned one-dimensional wavelet analysis. The velocity fields in the measurement plane can be expressed by:

$$v(x_i, y_j, n) = \overline{v(x_i, y_j)} + \underbrace{W^T S_1(x_i, y_j)}_{\text{Level 1}} + \underbrace{W^T S_2(x_i, y_j)}_{\text{Level 2}} \cdots + \underbrace{W^T S_i(x_i, y_j)}_{\text{Level } i} + \cdots + \underbrace{W^T S_{N-2}(x_i, y_j)}_{\text{Level } N-2} \quad (7)$$

### 3.2 Proper orthogonal decomposition

The Proper orthogonal decomposition (POD) is a technique to obtain a modal decomposition of a given ensemble of data in terms of the energy content. The classical POD based on two-point spatial correlation was first introduced by Lumley (1967) for the identification of coherent structures. The main target of POD is to find optimal representation of field realizations from an energetic point of view. It consists of seeking a function  $\phi(x)$  that maximizes the projection of the field component  $u(x, t)$  in a mean square sense. This maximization leads to a Fredholm integral equation:

$$\int R_{ij}(x, x') \phi_j^n(x') dx' = \lambda_i \phi_i^n(x) \quad (8)$$

where the  $x$  is space variable and  $R(x, x')$  is the time-averaged two-point spatial correlation tensor:

$$R_{ij}(x, x') = \overline{u_i(x) u_j(x')} \quad (9)$$

where  $x$  denotes the space variable and the over bar corresponds to the time-averaged operation. The eigenvalue problem has a finite set of POD basis that composed of empirical eigenfunctions  $\phi_i^n(x)$  ( $n = 1, \dots, N_{\text{mod}}$ ), here the  $N_{\text{mod}}$  denotes the total number of POD modes. This is the main principle of the so-called classical proper orthogonal decomposition. The instantaneous field component can be projected onto the POD basis by:

$$u_i(x, t) = \sum_{n=1}^{N_{\text{mod}}} a_n(t) \phi_i^n \quad (10)$$

This approach is normally applied to the data measured with a well-defined time description but with limited spatial resolution (e.g., Hot-wire Anemometry and Laser Doppler Anemometry). This is because that the size of the eigenvalue problem depends on the number of spatial points in which the measured field is available. When dealing with the PIV measurement technique, the measured data have good spatial resolution and poor temporal resolution. In such case, the so-called snapshot approach developed by Sirovich (1987) is normally used as it decreases the dimension of the eigenvalue problem from the number of spatial points to the number of time steps (snapshots). In this study, the snapshot POD approach was employed to extract turbulent structures measured by PIV experiment, and the calculation procedure is briefly describe as follow.

To perform snapshot POD analysis, the calculated fluctuating velocity components  $v'(x_i, y_j, t_n)$  were assembled into a single matrix  $U$  with the size of  $2 n_x n_y \times n_t$ :

$$U = [v'(:, 1) \quad v'(:, 2) \quad \cdots \quad v'(:, n_t)] = \begin{bmatrix} U'(1, 1) & U'(1, 2) & \cdots & U'(1, n_t) \\ U'(2, 1) & U'(2, 2) & \cdots & U'(2, n_t) \\ \vdots & \vdots & \vdots & \vdots \\ U'(n_x n_y, 1) & U'(n_x n_y, 2) & \cdots & U'(n_x n_y, n_t) \\ V'(1, 1) & V'(1, 2) & \cdots & V'(1, n_t) \\ V'(2, 1) & V'(2, 2) & \cdots & V'(2, n_t) \\ \vdots & \vdots & \vdots & \vdots \\ V'(n_x n_y, 1) & V'(n_x n_y, 2) & \cdots & V'(n_x n_y, n_t) \end{bmatrix} \quad (11)$$

In the resulting matrix  $U$ , the symbol “:” denotes that the instantaneous fluctuating velocity at one snapshot is rearranged into a column vector, the first  $n_x n_y$  elements of each column correspond to the instantaneous streamwise fluctuating velocity field, and the last  $n_x n_y$  elements are the corresponding vertical fluctuating velocity field. Considering each row of matrix  $U$ , the elements correspond to time sequences of fluctuating streamwise or vertical velocity components at one point.

The computation of snapshot POD modes requires solving eigenvalue problem of a covariance matrix  $R$  is given by:

$$R = U^T U \quad (12)$$

$$R A^i = \lambda^i A^i \quad (13)$$

It is evident that the covariance matrix  $R$  covers the approximated spatial data by the summation of snapshots. The solution of Eq. (13) consists of eigenvector  $A^i$  and its corresponding eigenvalue  $\lambda^i$ . Since the eigenvalue represents the energy contained in each POD mode, the eigenvectors are arranged according to the descending order of eigenvalues ( $\lambda^1 > \lambda^2 > \lambda^3 \dots > \lambda^{n_t} = 0$ ), then the POD modes are constructed by the ordered eigenvectors:

$$\phi^i = \frac{\sum_{n=1}^{n_t} v'(:, n) A_n^i}{\left\| \sum_{n=1}^{n_t} v'(:, n) A_n^i \right\|}, (i = 1, \dots, n_t) \quad (14)$$

The relative fluctuating kinetic energy associated with the  $i$ th POD mode can be computed as:

$$E^i = \frac{\lambda^i}{\sum_{i=1}^{n_t} \lambda^i}, (i = 1, \dots, n_t) \quad (15)$$

The projection of the fluctuating velocity components onto the POD modes provides time independent coefficients  $a_i$  for its corresponding POD mode:

$$a^n = \Phi^T v'(:, n) \quad (16)$$

where the matrix  $\Phi$  is made by arranging the POD modes  $\phi^i$  as column vectors. The POD modes provide spatial information of the physical structures cascading in terms of their energy content. However, the magnitudes of the modes are not enough to perform quantitative analysis unless combined with the POD coefficients to reconstruct the velocity fields. The fluctuating velocity components can be reconstructed as a linear combination of temporal coefficients and POD modes,

$$v'(:, n) = \sum_{i=1}^{n_t} a_i^n \phi^i \quad (17)$$

Similar to the one-dimensional wavelet multi-resolution analysis, the instantaneous flow fields can be reconstructed by:

$$v(x_i, y_j, n) = \overline{v(x_i, y_j)} + \underbrace{a_1^n \phi^1(x_i, y_j)}_{\text{Mode 1}} + \underbrace{a_2^n \phi^2(x_i, y_j)}_{\text{Mode 2}} + \dots + \underbrace{a_i^n \phi^i(x_i, y_j)}_{\text{Mode } i} + \dots + \underbrace{a_{n_t}^n \phi^{n_t}(x_i, y_j)}_{\text{Mode } n_t} \quad (18)$$

## 4 Results and discussion

### 4.1 Time-averaged flow field and spectral analysis

The spatial distributions of time-averaged streamlines, streamwise velocity, vertical velocity, Reynolds shear stress and turbulent kinetic energy (TKE) are obtained by averaging 15,000 instantaneous velocity fields, here the first and second order turbulent statistics are normalized by  $U_0$  and  $U_0^2$  respectively. As shown in Fig. 2a, two distinct regions of reverse flow behind the triangle cylinder are clearly identifiable, characterized by a pair of similar-sized vortices with opposite sense of rotation and a stagnation point on the centerline of triangle cylinder ( $y/L = 0$ ). The distance from the backside of triangle cylinder to the stagnation point is about  $1.7 L$ . Besides, two well-defined foci points are observed at the location about  $x/L = 0.75$ , with a vertical distance of  $0.7 L$  between them. The contour of time-averaged streamwise velocity appears to be symmetric with respect to the centerline. The minimum value occurs at the near center of



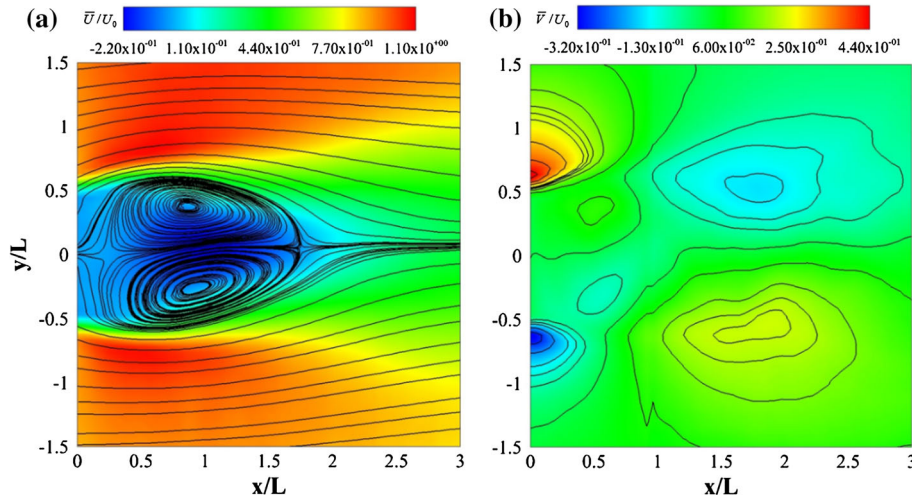


**Fig. 2** Time-averaged flow field. **a** Streamlines and contour of streamwise velocity, **b** contour of vertical velocity

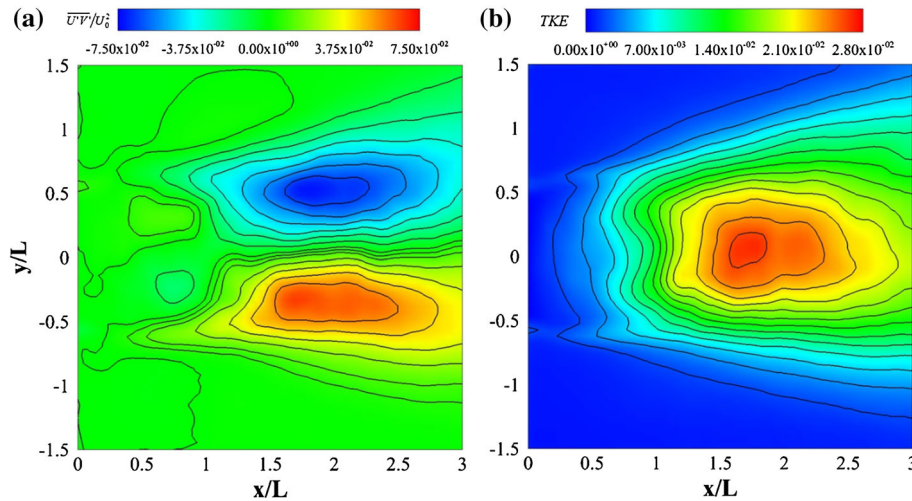


**Fig. 3** Second order statistics **a** Contour of Reynolds shear stress, **b** contour of turbulent kinetic energy

separation region, and it gradually increase to 0 at the stagnation point. The time-averaged vertical velocity contour is shown in Fig. 2b, and the antisymmetric distribution might indicate the entrainment between wake and main flow. The highest entrainment is originated from the two sides of triangle cylinder where the shear layer develops. The contours of Reynolds stress and turbulent kinetic energy are presented in Fig. 3. Similar to Fig. 2b, the Reynolds shear stress distribution (Fig. 3a) displays a pair of peak on either side of centerline near the end of the separation region. Between the shear layer and the backside of triangle cylinder, a region with notably weaker Reynolds shear stress is observed, indicating smaller velocity fluctuations in the near wake region. As presented in Fig. 3b, the turbulent kinetic energy gradually increases along downstream until reaches its maxima near the stagnation point, then it decreases gradually along the downstream direction. It may imply that maximum velocity fluctuations occur in the region close to the stagnation point due to the merging of shear layers.

The spectral characteristics of velocity components provide global frequency information of flow oscillations, in the wake region, and the dominating vortex shedding frequency can be determined by power spectra of the measured velocity data at several selected points. As shown in Fig. 4, FFT power spectra of vertical velocity was calculated at two locations ( $x/L = 0.8$  and  $x/L = 1.2$ ) with four points along the vertical direction, and the spectra  $S_v$  is plotted versus Strouhal number ( $S_t = fL/U_0$ ). As can be seen, the power spectra distributions have similar tendency at two locations along the vertical direction, for all

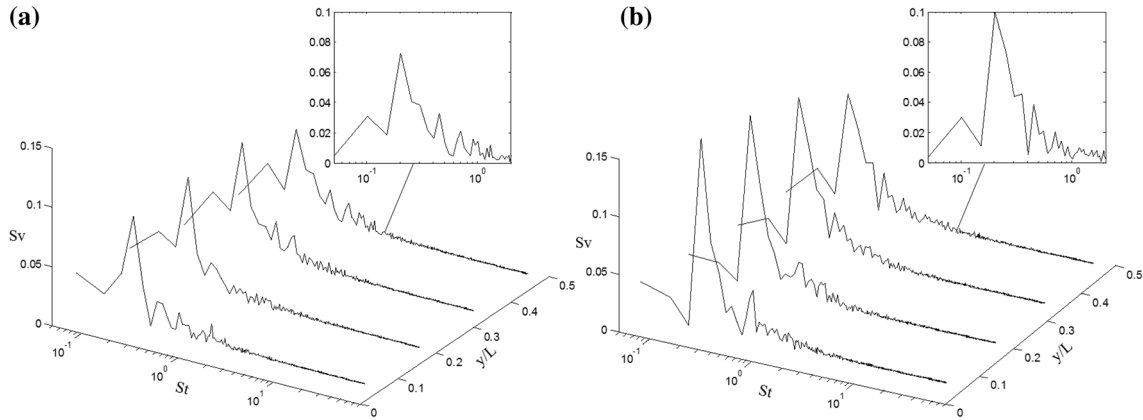


**Fig. 4** Vertical velocity spectra at selected points **a**  $x/L = 0.8$ , **b**  $x/L = 1.2$

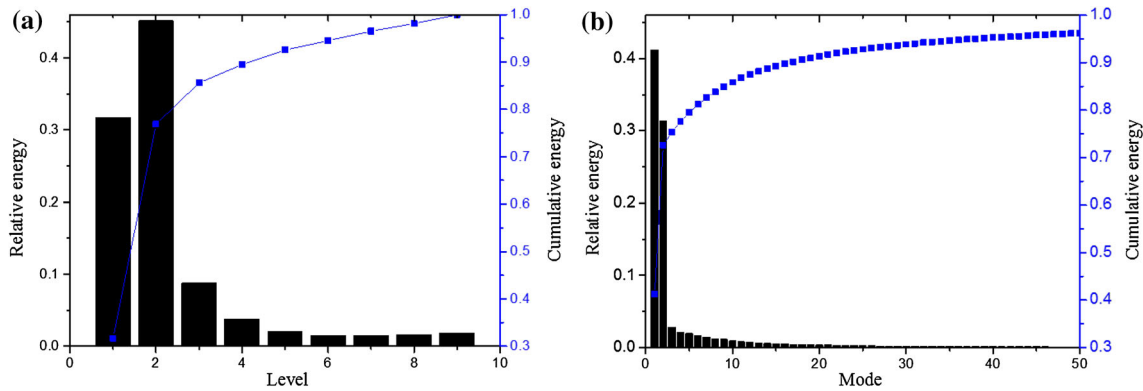


**Fig. 5** Energy distribution **a** Distribution of wavelet components, **b** distribution of POD modes

selected points, the pronounced peaks are observed at around  $St = 0.21$ , suggesting quasi-periodical vortex movement, namely the associating vortex shedding frequency. The peak spectrum magnitudes at location  $x/L = 1.2$  (Fig. 4b) are larger than that at location  $x/L = 0.8$  (Fig. 4a), indicating higher fluctuations at further downstream position within the separation region. Besides, it should be noted that second peaks of the spectra  $S_v$  are observed with corresponding  $St = 0.46$ , approximately twice of the first peak, implying the existence of relatively small-scale vortices.

#### 4.2 Energy distribution of wavelet components and POD modes

As discussed in Sect. 3.2, the normalized eigenvalue corresponds to the contribution of each mode to the total kinetic energy in the measurement plane. Similar to this calculating method, the energy of each wavelet component is first calculated by integrating kinetic energies over the measurement domain, and then the relative energy is normalized by the sum of energy contained in each wavelet component. Figure 5 shows the energy distribution of wavelet components and POD modes, here the left y axis is relative energy presented with bars, the right y axis represents cumulative energy, and the x axis represents the level of wavelet component or POD mode. As shown in Fig. 5a, the first four wavelet components contain 88 % of the total kinetic energy, and the wavelet components of level 1 and 2 makes the largest contribution, accounting for 32 and 45 %, respectively. It indicates that first two levels of wavelet components can be associated with the large-scale turbulent structure, which is apparently the uppermost and energy-containing structure. Figure 5b presents the energy distribution of first 50 POD modes (about 2.44 % of the total POD modes). As expected, the first two POD modes are most energetic, containing 73 % of the total kinetic energy (first and second modes contribute 41 and 32 %, respectively). However, the energy content of modes 3 and 4 reduces rapidly to 2.8 and 2.1 %, and the energy contained in rest modes makes less



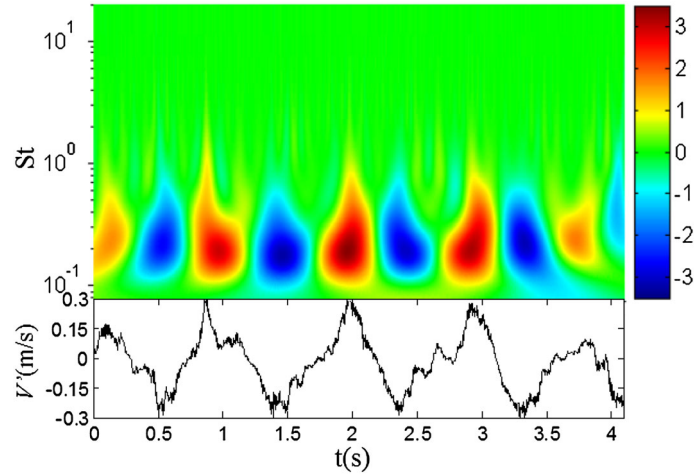


**Fig. 6** Continuous wavelet transform of vertical fluctuation velocity  $v'$  at  $x/L = 1.2$ ,  $y/L = 0.48$

contribution with increasing mode number. The energy concentration on first two modes suggests that the vortex shedding process can be linked to the first two modes.

From Fig. 5, it is found that the energy distribution of first two wavelet components has similar tendency with first two POD modes, indicating they are capable of extracting dominating turbulent structures. However, we should note that wavelet components give a representation of turbulent structure characterized by their frequency band widths, while the POD modes are classified based on the energy contained in each mode. The different classification criterion may result in different dynamic characteristics contained in wavelet components and POD modes. The detailed analyses will be carried out in the following subsection.

#### 4.3 Time–frequency analysis

The continuous wavelet transform has been widely applied to time series of signal due to its unique ability of revealing temporal information of energetic event together with its spectral information. To analyze the time frequency characteristics of wavelet components and POD modes, the continuous wavelet transform using Mexican Hat function as the mother wavelet is used in this study. The results are displayed on the time frequency planes, where the abscissa is the time  $t$ , and the ordinate is the normalized frequency of Strouhal number. The color mappings have been assigned to the wavelet coefficients and the highest concentration is displayed as red and the lowest as blue, respectively.

Figure 6 shows time–frequency distributions of coefficients of continuous wavelet transform at a selected point ( $x/L = 1.2$ ,  $y/L = 0.48$ ), and the corresponding time series of vertical fluctuating velocities are plotted at the bottom of Fig. 6. It is found that the fluctuating velocities exhibit quasi-periodical oscillations at around a corresponding Strouhal number  $St = 0.21$ , where alternative negative and positive peaks are observed. The peaks around  $St = 0.21$  correspond to the frequency of large-scale vortices, which can also be observed in Fig. 4. It is obvious that such vortical components contain most energy of velocity fluctuation. Besides, some peaks are also observed in the range of  $St = 0.5–2.5$ , which may represent the relatively small-scale eddies.

As discussed in Sect. 3, the fluctuating velocity components can be expressed by linear combination of wavelet components or POD modes. As is known, the turbulence manifests itself as a multi-scale cascading phenomenon superimposed on a mean flow. The reconstruction procedure of wavelet and POD analyses enable us to extract more detailed turbulent structures of real flow field that may reflect in different physical properties.

In order to reveal frequency behavior of the possibly existed flow phenomena, continuous wavelet transform was applied to the wavelet components and POD modes of vertical velocity at a selected point ( $x/L = 1.2$ ,  $y/L = 0.48$ ). Figure 7 shows time–frequency distributions of first six levels of wavelet components and their corresponding time-varying coefficients. It is evident that coefficients of levels 1 and 2 possess larger fluctuating amplitudes than those of higher levels (level 3, 4, 5 and 6). Besides, a quasi-periodical oscillation is clearly observed by level 2, implying its ability for representing vortex shedding behavior. Concerning the time frequency distribution, it can be seen that the dominating frequency increases with

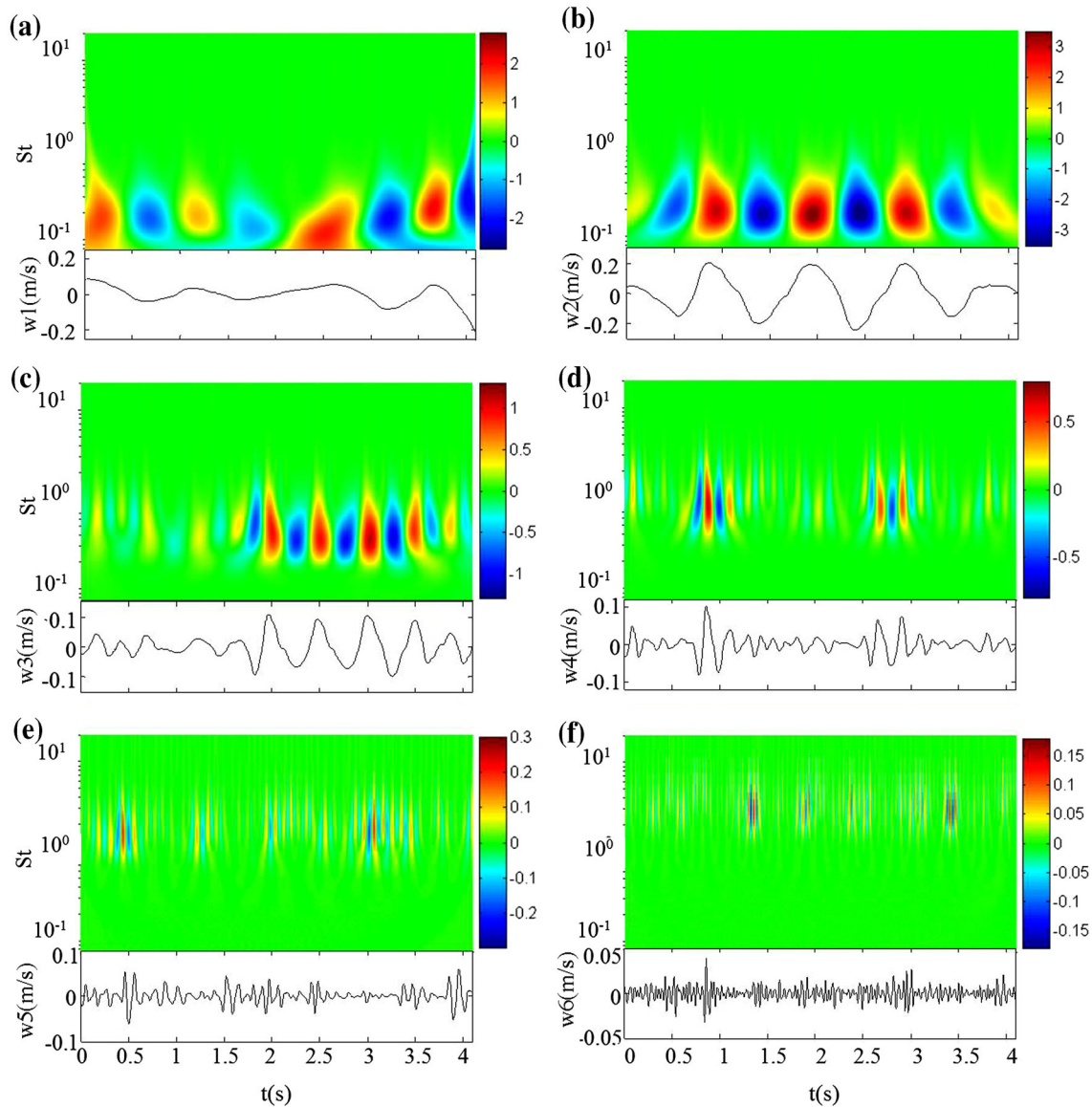


**Fig. 7** Continuous wavelet transform of wavelet components at  $x/L = 1.2$ ,  $y/L = 0.48$ . **a** Level 1, **b** level 2, **c** level 3, **d** level 4, **e** level 5, **f** level 6

increasing level number, the corresponding Strouhal number are observed at  $S_t \approx 0.17, 0.2, 0.42, 0.8, 1.5$  and 3 by level 1, 2, 3, 4, 5 and 6, respectively. On the contrary, the fluctuating energy of last five wavelet components (level 2–6), which can be described by the coefficients of continuous wavelet transform, decreases as increasing frequency. It implies that the frequency behavior of fluctuating velocity is dominated by wavelet components of low frequency, which can be associated with the dynamics of large-scale vortices. The wavelet components of relatively high frequency, as shown in Fig. 7c, d, have good correspondence to the frequency components ranging from 0.3 to 1.0 (see Fig. 4), indicating the capacity of the wavelet analysis to extract small-scale structures. The wavelet components of levels 3 and 4 can be linked to small-scale structures. As for levels 5 and 6, no evident structures can be found due to the lower energy content and higher frequency of them. The time frequency distributions of first six POD modes and their corresponding time-varying coefficients are shown in Fig. 8. It can be clearly seen that coefficients of first two modes have sinusoidal variations, with a nearly same period and a phase shift of a quarter of period. This confirms the correspondence between first two modes and vortex shedding behavior. Comparing with the coefficients of wavelet components, the first two POD modes have stronger periodicity than those of first two wavelet components. As for the coefficients of higher modes, periodical variation is weakened and no

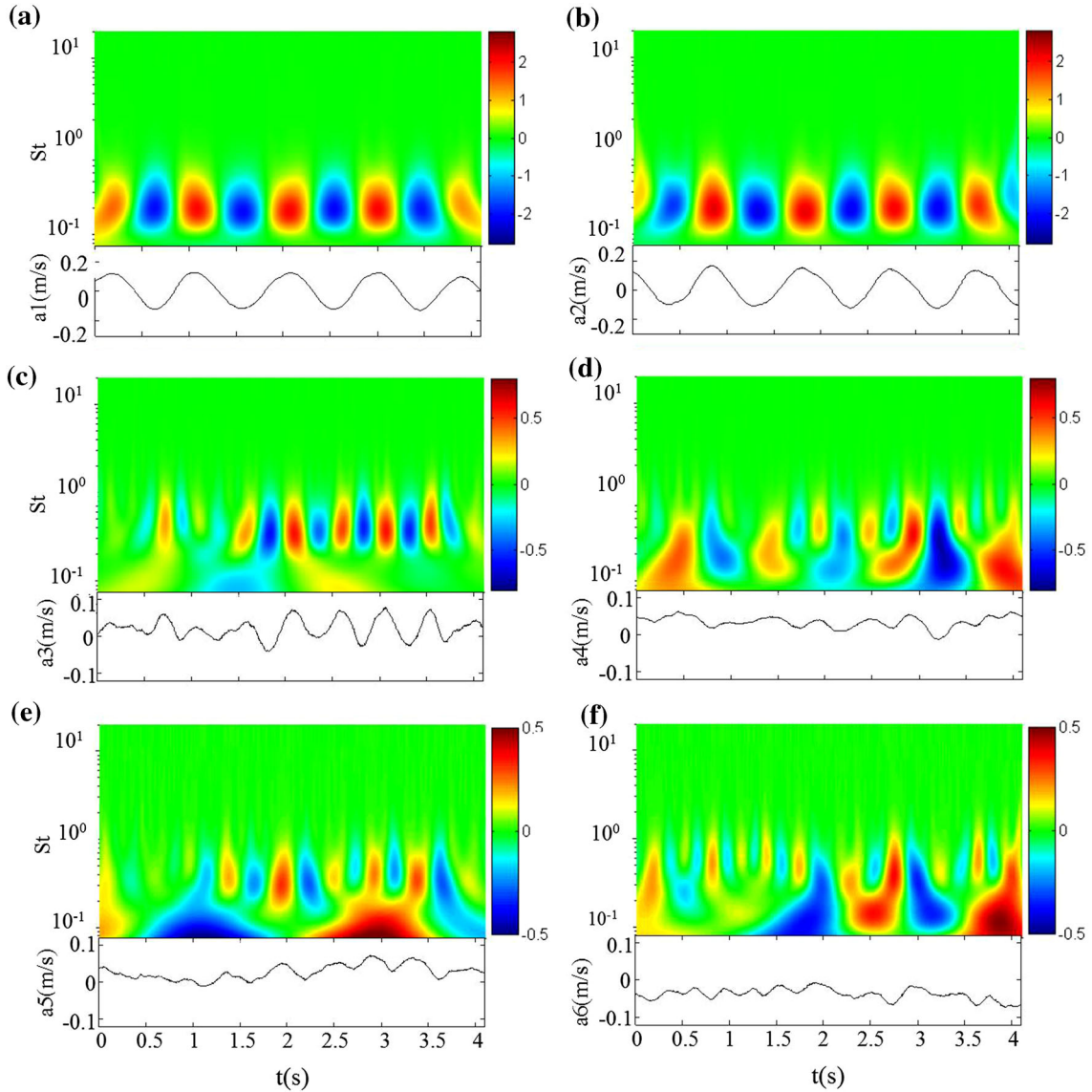


**Fig. 8** Continuous wavelet transform of POD modes at  $x/L = 1.2$ ,  $y/L = 0.48$ . **a** Mode 1, **b** mode 2, **c** mode 3, **d** mode 4, **e** mode 5, **f** mode 6

evident periodicity is observed. Concerning the time frequency distribution, it is observed that the first two modes (Fig. 8a, b) are most energetic, having strong quasi-periodical characteristics at a corresponding Strouhal number of 0.21. This further confirms that the first two modes are related to the fundamental frequency of vortex shedding and they are able to give representations of the dominant Karman-like vortices.

Considering the higher POD modes, Fig. 8c–f does not exhibit evident periodical behaviors. The corresponding Strouhal numbers are observed in a wider range, and the higher frequency components ( $S_t = 0.35\text{--}0.75$ ) may associate with small-scale eddies. The lower frequency components ( $S_t = 0.08\text{--}0.13$ ) may be due to unsteady flow motion induced by Karman-like vortex shedding behavior (Lee and Miao 2012), and they are not the dominant structures.

In general, the first two wavelet components and POD modes are capable of extracting the most energetic large-scale structures. Comparing with the wavelet components, the first two POD modes tend to be more appropriate to represent the Karman-like vortical structures due to their strong quasi-periodical behaviors. The small-scale eddies can be successfully extracted by wavelet components of levels 3 and 4 as the distinct classification of dominating frequencies by wavelet analysis. The lower frequency components

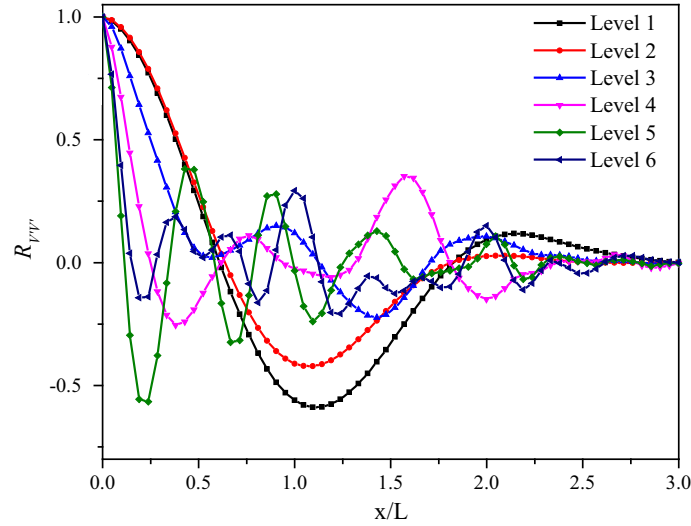


**Fig. 9** Two-point correlation of wavelet components

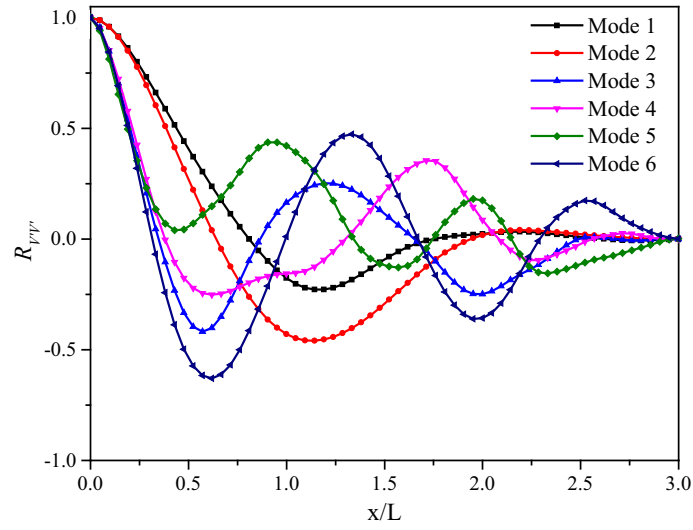
contained in higher POD modes seems to be superimposed on the wavelet component of level 1 (Fig. 7a), and this can be inferred as a reason why the energy content of first two wavelet components is larger than that of first two POD modes.

#### 4.4 Scale characteristics of wavelet components and POD modes

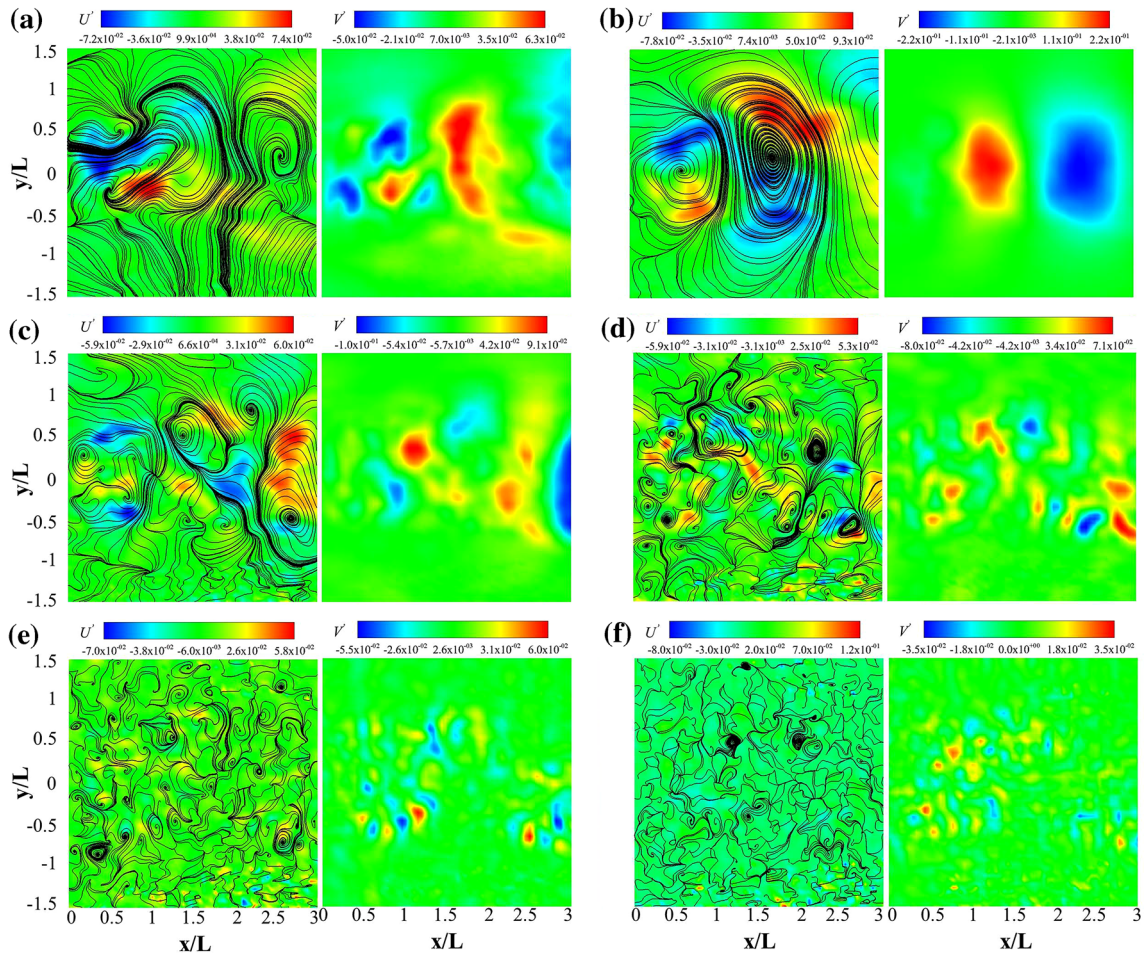
The time–frequency behaviors of wavelet components and POD modes have been discussed in the above subsection, however, the corresponding scale characteristics are still unknown. In order to determine the scale length of both, we computed two-point correlation function for each wavelet component and POD mode. Taking the wavelet components of vertical fluctuating velocity as an example, the two-point correlation coefficient is defined as  $R_{V^i V^i}^i(x, r) = \frac{V^i(x)V^i(x,r)}{\sqrt{(V^i)^2(x)(V^i)^2(x,r)}}$ , where  $V^i$  is fluctuating vertical velocity, the superscript  $i$  ( $i = 1, \dots, 6$ ) denotes fluctuating velocities of different level, and  $r$  is the separation between two points along streamwise direction.

Figure 9 presents correlation function of wavelet components at the location of  $y/L = 0$  along the streamwise direction. It is evident that all the coefficients reduce to their first minimums and continue oscillating before they become zero at about  $x/L = 2.8$ , the length scales of  $x/L \approx 2.2, 2.0, 0.9, 0.75, 0.5$  and  $0.36$  are observed by wavelet components from level 1 to 6, respectively, and the length scale decreases with increasing frequency. The first two wavelet components can give representation of large-scale structures, and wavelet components of levels 3 and 4 can be regarded as small-scale structures. The wavelet components of levels 5 and 6 may contain some random and noisy events. These observations may indicate that multi-scale vortical structures are organized by the components characterized by their dominant frequencies. The length scales of first two wavelet components confirm the fact that low-frequency components are associated with large-scale vortical structures, and the larger length scale of first wavelet component may suggest that the unsteady flow motion induced by Karman-like vortex shedding behavior results in the generation of relatively larger vortical structures. The scale characteristics of wavelet components suggest that the frequency behavior can reflect the spatial-related length scale of vortical structure and the wavelet analysis provides a tool for extracting vortical structures of different scale. The coefficients of POD modes are shown in Fig. 10, the length scales of first two POD modes are nearly the same with the value of  $x/L \approx 2.1$ , indicating the length scale of Karman-like large-scale vortical structure. As for higher POD modes, the length scale of  $x/L \approx 1.15, 1.75, 0.85$  and  $1.3$  are observed by POD mode 3, 4, 5 and 6, respectively. Different with wavelet components, no evident relationship between POD mode and length scale can be found. This is because wider range of frequency contained in POD modes. Concerning the result of POD analysis, the first two modes give a good representation of Karman-like vortical structure due to the frequency and length scale characteristics of them. However, it is difficult to extract small-scale





**Fig. 10** Two-point correlation of POD modes



**Fig. 11** Velocity contours and streamline patterns of wavelet components. **a** Level 1, **b** level 2, **c** level 3, **d** level 4, **e** level 5, **f** level 6

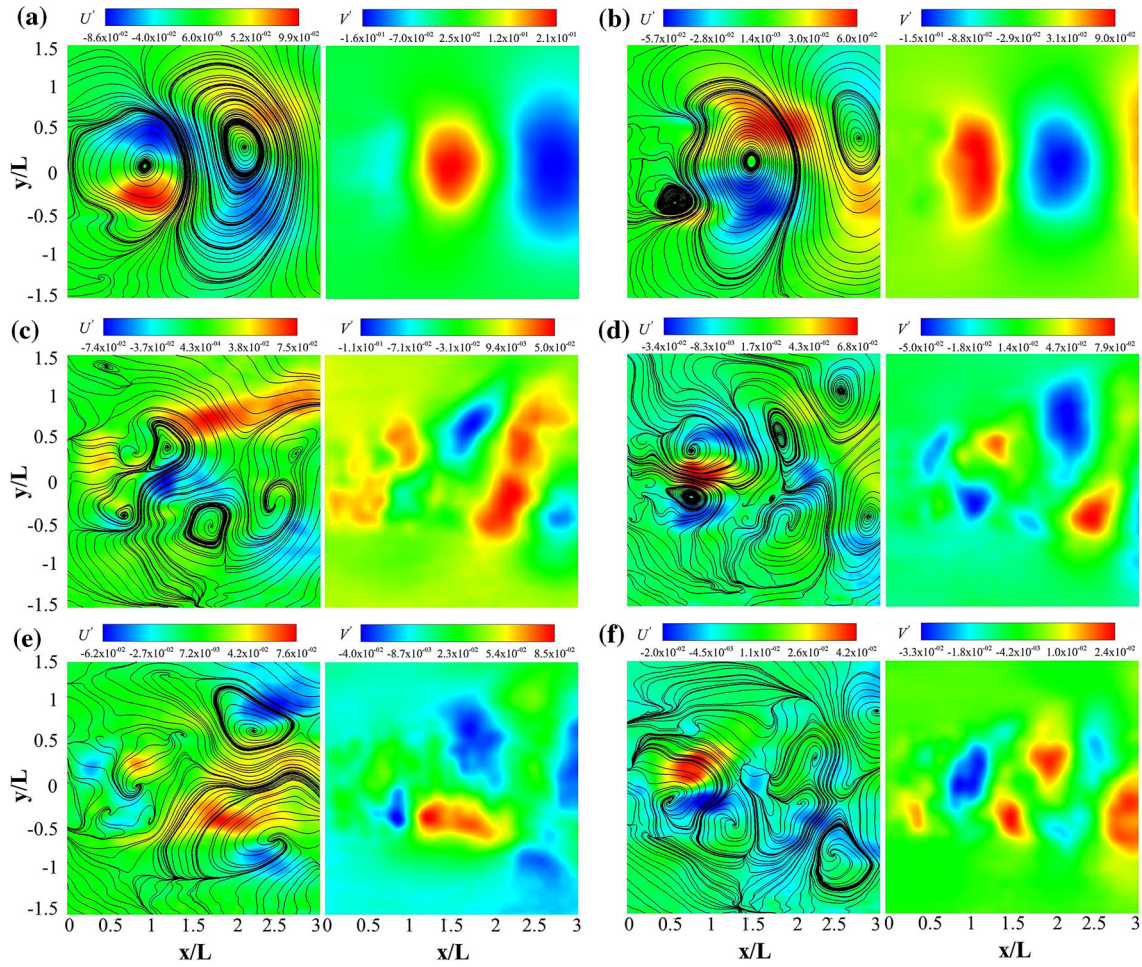


**Fig. 12** Velocity contours and streamline patterns of POD modes. **a** Mode 1, **b** mode 2, **c** mode 3, **d** mode 4, **e** mode 5, **f** mode 6

vortical structures as the fluctuation velocity components are irregularly classified in frequency and spatial domain.

#### 4.5 Flow patterns of wavelet components and POD modes

The representative flow patterns of wavelet components and POD modes are presented in Figs. 11 and 12, in each of the subfigure, the left part contains the streamwise velocity ( $U'$ ) contour and the right part the vertical velocity ( $V'$ ) contour, to interpret the wavelet components and POD modes in terms of flow patterns, the corresponding streamlines are plotted in the left part of each subfigure. As shown in Fig. 11, it is evident that spatial scale decreases as increasing level number, which is in accordance with the results presented in Fig. 9. The relatively small-scale structures are clearly identifiable in Fig. 11c–e, indicating that wavelet transform is able to extract multi-scale turbulent structures. As for Fig. 11f, no evident vortical structures can be observed, the flow pattern of level 6 may be linked to random or noisy event contains in the flow field. As can be seen in Fig. 12a, b, the streamwise velocity appears symmetrically about the centerline, while the vertical velocity appears anti-symmetrically about the centerline. The streamline patterns of first two modes are similar in shape, and the structure of mode 2 appears to displace downstream to the structure of mode 1. This feature is attributed to the quasi-periodical nature of the wake flow. Concerning the higher POD modes, it is difficult to find the correspondence between mode pairs (i.e. modes 1 and 2, modes 3 and 4). Compared with the first two POD modes, no evident linkage between level 1 (Fig. 11a) and level 2 (Fig. 11b) can be found, this further confirm that first two POD modes are more appropriate to represent the Karman-like vortical structures.



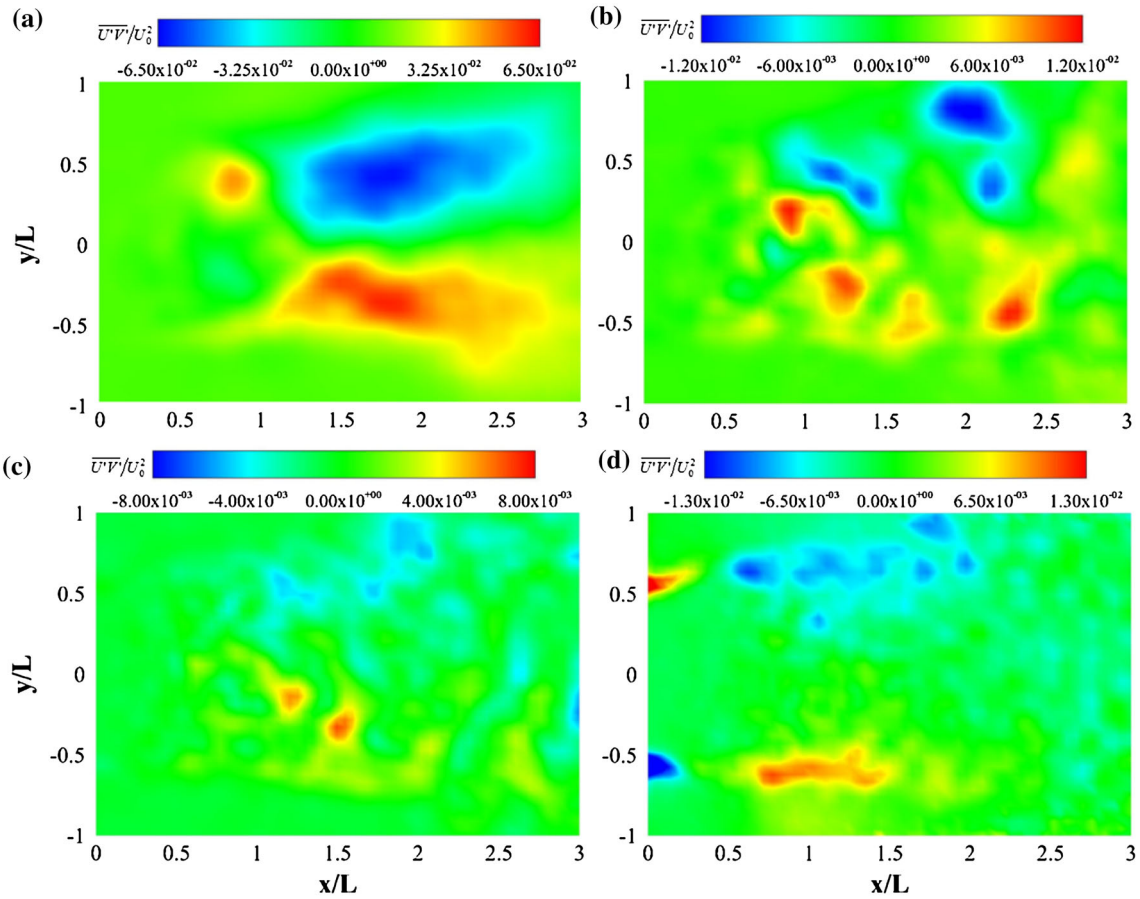


**Fig. 13** Contours of normalized Reynolds shear stress for each wavelet component: **a** Level 1 + 2; **b** level 3; **c** level 4; **d** level 5+

#### 4.6 Reynolds shear stresses of wavelet components and POD modes

As mentioned above, the wavelet components and POD modes enable us to extract the flow structures that possibly buried in the mean flow. It would be interesting to analyze the corresponding Reynolds stress based on the reconstructed fluctuating velocities. To calculate the Reynolds stresses, the reconstructed fluctuating velocities are rearranged into four parts: the first part is constructed by adding the first two wavelet components or POD modes together as they give good descriptions of large-scale vortical structure, the second and third parts are the corresponding fluctuating velocities of levels 3 and 4 or POD mode 3 and 4, and the rest part of fluctuating velocities corresponds to the fourth part.

Figure 13 shows the distributions of rearranged Reynolds shear stresses of wavelet components of above-mentioned four parts. From Fig. 13a, it can be seen that the maximum Reynolds shear stress appearing near the end of the separation region, and coincides approximately with that in Fig. 3a associated with large-scale structure, contributes about 88 % of the measured Reynolds shear stress. It indicates that the most significant contribution to the Reynolds stresses comes from the coherent motions of large-scale structures. Similar to the fluctuating energy distribution, the maximum values of Reynolds shear stress decrease when the wavelet components increase to levels 3 and 4 (Fig. 13b, c). Besides, the spatial distribution of level 3 exhibits larger scale than level 4, which further confirms the decrease of spatial scale with increasing frequency. Concerning the result of the rest wavelet components (Fig. 13d), the maximum value of Reynolds shear stress is larger than that of levels 3 and 4, because that the higher frequency components are added together with larger fluctuating energy. Furthermore, it is worthy to note that two antisymmetric region of Reynolds shear stress distributions are observed near the body surface and the boundary of separation region. It suggests that there is an intensive velocity fluctuation with higher frequency in the shear layer. Figure 14 presents the distributions of rearranged Reynolds shear stresses of POD

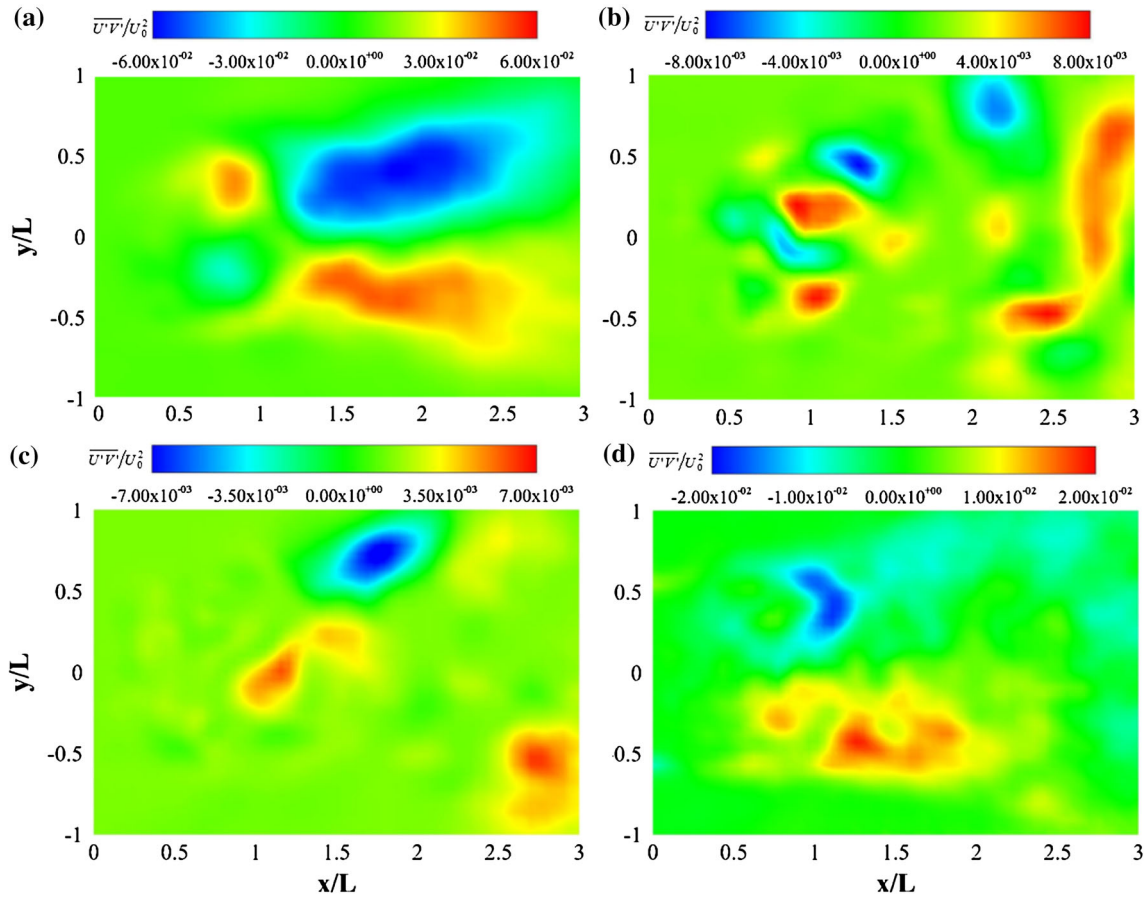


**Fig. 14** Contours of normalized Reynolds shear stress for each POD mode: **a** Mode 1 + 2; **b** mode 3; **c** mode 4; **d** mode 5+

modes of above-mentioned four parts. As expected, the Reynolds shear stress distribution in Fig. 14a shows good correspondence to that in Fig. 3a, accounting for 80 % of the measured Reynolds shear stress. It indicates that Karman-like vortical structures dominate the variations of Reynolds shear stresses. Due to the descending ordered fluctuating energy, the maximum values of Reynolds shear stress decreases from POD mode 3 to mode 4 (Fig. 14c, d), and no distinct difference of spatial scale is observed between them. Different with the result in Fig. 11d, the Reynolds shear stress distribution of rest POD modes (Fig. 14d) is observed in the separation region. This is due to wider range of frequency components contained in the rest POD modes, indicating that lower frequency also plays a role in velocity fluctuations in the separation region although they are not dominant.

## 5 Conclusions

One-dimensional orthogonal wavelet and POD analyses are combined to extract multi-scale flow phenomena in this study. The features of reconstructed flow fields are analyzed in terms of fluctuating energy, time–frequency distribution, space correlation and Reynolds shear stress. The main results are summarized as follows.

1. The first two wavelet components and POD modes are most energetic, contributing about 77 and 73 % to the total fluctuating energy, respectively. The energy distributions of them indicate that they are capable of extracting dominating large-scale turbulent structures.
2. Compared with POD modes, the central frequencies of wavelet components are distinctly classified as the band pass filter process of orthogonal wavelet transform. The time–frequency analyses suggest that the first two POD modes are more appropriate to represent the Karman-like vortical structures due to

their strong quasi-periodical behaviors at  $S_t = 0.21$ . When increasing to higher modes, poor filtering effects in the range of lower frequency ( $S_t = 0.08\text{--}0.13$ ) is observed, and the lower frequency components are considered to be superimposed on the wavelet component of level 1. This can be inferred as a reason why the energy content of first two wavelet components is larger than that of first two POD modes.

3. The length scale of wavelet components is found to decrease with the increasing frequency, suggesting that the frequency behavior can reflect the spatial-related length scale and the wavelet analysis can be used to extract turbulent structures of different scales.
4. The first two POD modes have nearly same length scale of  $x/L = 2.1$ , as for higher POD modes, no evident relationship between POD mode and length scale can be found, which is different from the wavelet components. This further confirms that the first two modes give a good representation of Karman-like vortical structure due to the frequency and length scale characteristics of them. However, it is difficult to extract small-scale turbulent structures as the fluctuation velocity components are irregularly classified in frequency and spatial domain.
5. The most significant contributions to the Reynolds shear stresses are attributed to coherent motions of large-scale structures that composed of first two wavelet components and POD modes, accounts for 88 and 80 % of the measured maximum Reynolds shear stress, respectively. The higher wavelet components and POD modes corresponding to random motions make less contribution to Reynolds shear stresses.
6. The different dynamic characteristics contained in wavelet components and POD modes are due to different classification criterion of these two methods, and the combining use of these two methods tends to be more effective for analyzing multi-scale turbulent structures.

## References

- Addison PS, Murray KB, Watson JN (2001) Wavelet transform analysis of open channel wake flows. *J Eng Mech* 127(1):58–70
- Alam MD, Zhou Y (2008) Strouhal numbers, forces and flow structures around two tandem cylinders of different diameters. *J Fluids Struct* 24:505–526
- Cazemier W, Verstappen RWCP, Veldman AEP (1998) Proper orthogonal decomposition and low dimensional models for driven cavity flows. *Phys Fluids* 10(7):1685–1699
- Cruz AS, David L, Pécheux J, Texier A (2005) Characterization by proper-orthogonal-decomposition of the passive controlled wake flow downstream of a half cylinder. *Exp Fluids* 39(4):730–742
- Davis RW, Moore EF, Purtell LP (1983) A numerical–experimental study of confined flow around rectangular cylinders. *Phys Fluids* 27:46–59
- Delville J, Ukeiley L, Cordier L, Bonnet JP, Glauser M (1999) Examination of large-scale structures in a turbulent plane mixing layer. Part 1. proper orthogonal decomposition. *J Fluid Mech* 391:91–122
- Durgesh V, Naughton JW, Whitmore SA (2013) Experimental Investigation of base drag reduction via boundary layer modification. *AIAA J* 51(2):416–425
- Farge M, Pellegrino G, Schneider K (2001) Coherent vortex extraction in 3D turbulent flows using orthogonal wavelets. *Phys Rev Lett* 87:054501
- Graftieaux L, Michard M, Grosjean N (2001) Combining PIV, POD and vortex identification algorithms for the study of unsteady turbulent swirling flows. *Measur Sci Technol* 12:1422–1429
- Hussain AKMF, Hayakawa M (1987) Evolution of large-scale organized structures in a turbulent plane wake. *J Fluid Mech* 108:193–229
- Indrusiak MLS, Moller SV (2011) Wavelet analysis of unsteady flows: application on the determination of the Strouhal number of the transient wake behind a single cylinder. *Exp Thermal Fluid Sci* 35:319–327
- Lee HH, Miao JJ (2012) An investigation on Karman-type vortex shedding from a finite square cylinder. *J Mech* 28:299–308
- Lin JC, Vorobieff P, Rockwell D (1996) Space-time imaging of a turbulent near-wake by high-image-density particle image cinematography. *Phys Fluids* 8:555–564
- Lumley JL (1967) The structure of inhomogeneous turbulence. In: Yaglom AM, Tatarski VI (eds) *Atmospheric turbulence and wave propagation*. Nauka, Moscow, pp 166–178
- Mallat S (1989) A theory for multi resolution signal decomposition: the wavelet representation. *IEEE Trans PAMI* 11:674–693
- Noack B, Afanasiev K, Morzynski M, Tadmor G, Thiele F (2003) A hierarchy of low-dimensional models for the transient and post transient cylinder wake. *J Fluid Mech* 497:335–363
- Rinoshika A, Zhou Y (2005a) Orthogonal wavelet multi-resolution analysis of a turbulent cylinder wake. *J Fluid Mech* 524:229–248
- Rinoshika A, Zhou Y (2005b) Effects of initial conditions on a wavelet-decomposed turbulent near-wake. *Phys Rev E* 71(046303):1–8
- Sirovich L (1987) Turbulence and the dynamics of coherent structures, Part I Coherent structures. *Q Appl Math* 45:561–571
- Wang Y, Yu B, Wu X (2012) POD and wavelet analyses on the flow structures of a polymer drag-reducing flow based on DNS data. *Int J Heat Mass Transf* 55(17):4849–4861

- 
- Wei T, Smith CR (1986) Secondary vortices in the wake of circular cylinders. *J Fluid Mech* 169:513–533
- Weier T, Cierpka C, Gerbeth G (2008) Coherent structure eduction from PIV data of an Electro magnetically forced separated flow. *J Fluids Struct* 24:1339–1348
- West GS, Apelt CJ (1982) The effects of tunnel blockage and aspect ratio on the mean flow past a circular cylinder with Reynolds numbers between  $10^4$  and  $10^5$ . *J Fluid Mech* 114:361–377
- Williamson CHK (1996) Vortex dynamics in the cylinder wake. *Annu Rev Fluid Mech* 28:477–539
- Zdravkovich MM (1997) Flow around circular cylinders, vol 1. Oxford University Press, Oxford, Fundamentals